

Complex networks in brain electrical activity



Starlab Knowledge Nugget KN-2005-11-15, Kolmogorov project
Status: Starlab Preprint
Project Initiated: April 7th 2005

Authors: G. Ruffini¹, C. Ray, J. Marco, L. Fuentemilla, C. Grau

Date: Nov 15th 2005

Version: 1.8

Starlab Barcelona, S.L.

Edifici de l'Observatori Fabra, C. de l'Observatori s.n.

Muntanya del Tibidabo, 08035 Barcelona, Spain

[http:// starlab.es](http://starlab.es)

Summary

Keywords: Complex Networks, Electroencephalography (EEG), Event Related Potentials (ERP), Low Resolution Tomography (LORETA), Mismatch Negativity (MMN)

This paper is the result of work carried out at Starlab in collaboration with the Neurodynamics Laboratory of the U. of Barcelona (UBNL) focusing on complex networks analysis of EEG data (provided by UBNL). The approach is inspired by the work in [6] with fMRI data and represents a follow up on earlier efforts on analysis of ERP/MMN data using tomography and independent component analysis to characterize brain connectivity and spatial functionalization [22]. Multichannel EEG measurements are first processed to obtain 3D voxel activations using the tomographic algorithm LORETA. Then, the correlation of the current intensity activation between voxel pairs is computed to produce a voxel cross-correlation coefficient matrix. Using several correlation thresholds, the cross-correlation matrix is then transformed into a network connectivity matrix and analyzed. The resulting analysis highlights significant differences between the spatial activations associated with Standard and Deviant tones, with interesting physiological implications. When compared to random data networks, physiological networks are more connected, with longer links and shorter path lengths. Furthermore, as compared to the Deviant stimulus case, Standard data networks are consistently more connected, with longer links and shorter path lengths—consistent with a “small worlds” character. The comparison between both networks shows that areas known to be activated in the MMN wave are connected. In particular, the analysis supports the idea that supra-temporal and inferior frontal data work together in the processing of the differences between sounds by highlighting an increased connectivity in the response to a novel sound.

¹Contact: giulio.ruffini@starlab.es

Complex networks in brain electrical activity

G. Ruffini¹, C. Ray^{1,2}, J. Marco^{1,3}, L. Fuentemilla³, C. Grau³

¹Starlab, C. de l'Observatori, s/n, 08035 Barcelona, Spain, <http://starlab.es>

²Physics Department, St. Mary's College, Moraga, CA, USA

³Neurodynamics Laboratory, Department of Psychiatry and Clinical Psychobiology, University of Barcelona, Spain

Abstract

Keywords: Complex Networks, Electroencephalography (EEG), Event Related Potentials (ERP), Low Resolution Tomography (LORETA), Mismatch Negativity (MMN)

A major challenge for neuroscience is to map and analyze the spatiotemporal patterns of activity of the large neuronal populations which are believed to be responsible for information processing in the human brain. In this paper, we analyze the complex networks associated with brain electrical activity in a specific experimental context. Our approach uses multichannel EEG data analysis to characterize the spatial connectivity of the brain. Multichannel EEG measurements are first processed to obtain 3D voxel activations using the tomographic algorithm LORETA. Then, the correlation of the current intensity activation between voxel pairs is computed to produce a voxel cross-correlation coefficient matrix. Using several correlation thresholds, the cross-correlation matrix is then transformed into a network connectivity matrix and analyzed. To study a specific example, we selected data from an earlier experiment focusing on the Mismatch Negativity (MMN) brain wave— an Event-Related Potential (ERP)—because it gives an electrophysiological index of a “primitive intelligence” associated with auditory pattern and change detection in a regular auditory pattern. EEGs have an exceptional millisecond temporal resolution, but appear to result from mixed neuronal contributions whose spatial location and relationships are not fully understood. Although that experimental setup was not optimal for the purpose of tomography and network analysis (only 30 electrodes were used), the resulting analysis has already detected significant differences between the spatial activations associated with Standard and Deviant tones, with interesting physiological implications. As a cross-check, we have also analyzed the networks from randomly generated data. When compared to random data networks, physiological networks are more connected, with longer links and shorter path lengths. Furthermore, as compared to the Deviant stimulus case, Standard data networks are consistently more connected, with longer links and shorter path lengths— consistent with a “small worlds” character. The clustering index is rather high in general, especially in comparison to an equivalent random network. The departure from randomness is extreme at high thresholds. On the other hand, the clustering index does not appear to discriminate clearly the Standard and Deviant networks, while relative low correlation thresholds appear to be more discriminating. Yet, when compared to random or Deviant data, Standard data networks appear to fragment more easily, with the number of sub-networks increasing at larger thresholds. On the other hand, the comparison between both networks shows that areas known to be activated in the MMN wave are connected. In particular, the analysis supports the idea that supra-temporal and inferior frontal data work together in the processing of the differences between sounds by highlighting an increased connectivity in the response to a novel sound.

1 Introduction

The availability of large amounts of data and increasingly powerful computers is enabling the analysis of complex systems with many highly interconnected elements. Examples of such systems abound both natural and artificial, and include the cell, the brain, society, the internet, the behavior of crowds and the economy to name a few [2, 43]. The brain is perhaps the most interesting and complex of all such systems, with hundreds of billions of highly interconnected neurons. Complex networks theory provides a tool for the analysis of the connectivity of such complex systems, where interesting phenomena are emergent from a high number of highly interacting elements. It is therefore rather natural that this methodology will be put to practice intensely to study information processing in the brain at different scales.

While a complete analysis of the brain at cellular level is beyond present capabilities, we can analyze the function and connectivity of the brain at relatively small scales. One of the early views in neuroscience is that specific areas of the brain are specialized in performing specific tasks. This working hypothesis has led to the discovery of several functional properties of distinct areas by lesional, intracortical and neuroimaging studies. However, functional localization cannot be uncovered by the analysis of anatomical localization alone, as such an approach would not uncover functional interaction integration of different brain areas. Functional integration refers to an effective connectivity, that is, it depends on both connectivity dynamism and upon a model of interactions [7]. A more general model postulates the processing of information through cooperation of different localized regions.

Although several powerful functional approaches to image-specific neuronal assemblies while the human brain is functioning are available today [42], they all have a limited application niche. Some are invasive, while others are based on an indirect index of brain computing—such as metabolic or hemodynamic measurements which are blind to millisecond phenomena (Positron Emission Tomography, PET; and functional Magnetic Resonance, fMRI, for instance). In contrast to these methods, electromagnetic scalp brain activity techniques (Electroencephalography, EEG, Event- Related Potentials, ERP, and their magnetic counterparts) have the advantages of being non-invasive, of being closely related to the traffic of ions through the dendritic ion channels that are believed to support cerebral computing [18], and of having an exceptional temporal resolution (in the order of a millisecond). While these signals seem to be very rich in information, information extraction has been traditionally elusive [30]. In particular, the coarse spatial resolution of EEG has limited its impact. Traditionally, studies on this topic have focused in the connectivity of scalp electrodes. However, recent advances in the search for the sources of the brain electrical activity (the so-called inverse problem) have provided a foothold for the use of EEG to study the spatial connection between distant areas of the brain.

In [6] fMRI human brain data was analyzed using a complex networks approach, and evidence was found for a scale free behavior of the derived functional networks—basically the degree probability distribution obeyed a power law for high degrees. This paper seeks to analyze, in a similar vein, EEG data. EEG data is very complementary to fMRI data, which is metabolic in nature. EEG is a non-invasive technique with a high temporal resolution and a medium spatial resolution, as we discuss below. While fMRI measurements are readily available as 3D fields, EEG data is only measured at the scalp. Since our interest is focused on 3D localization of the networks associated with large neuronal groups, the first step in our approach is to tomographically “decode” electrode data and map it into 3D voxel activation data—the derived networks are then to reflect 3D spatial connectivity patterns.

In this paper we describe a “complex networks” methodology for electrophysiology and apply it to a relatively simple set of data obtained in an Event Related Potential protocol with

13 subjects and collected with 30 EEG channels. While is certainly true that 30 electrodes are barely sufficient to obtain good tomographic results, we aim here to carry out a first simple test of the approach. The technique can be applied with more sophisticated data sets, and the envisioned applications are many.

Our approach will be applied to a set of single trial ERP data in a Mismatch Negativity (MMN) paradigm [25]. MMN is a wave that appears 100-200 ms after the incoming of a tone that breaks the regularity of an stream of regular tones. In order to probe the structure of a particular functional brain network, we will consider in this study the impact produced by an environmental change. The brain can be studied as a pattern modeling tool, where inputs from the environment transduced by body sensors are analyzed. The capability to model ambient inputs is crucial for the survival of higher organisms. Neural networks responsible for this task determine whether incoming information needs to deeply alter brain dynamics (robustness) or to adjust (responsiveness), even dramatically, in order to effectively respond [3].

MMN reflects the capacity of the system to detect a sudden environmental change[27] which constitutes a fundamental ability to ensure the survival of the organism [41, 13]. MMN constitutes an auditory ERP that has been suggested to be a measure of auditory information pre- attentive processing [32, 14, 28], as one of the first stages of gating information to consciousness [13]. The MMN system has been suggested to reflect a “primitive intelligence” [29] that provides an in vivo simplified model for studying abstract brain processing and related memory mechanisms. The MMN wiring network includes several brain areas, as concluded from studies using diverse techniques (including EEG, fMRI and PET). It has been described to relate mostly to both supra- temporal hemispheres [1, 38, 13, 16, 24] and frontal areas [9, 31, 24, 4, 21], with a predominance of the right hemisphere, and also parietal sources [19, 20]. A step forward would be to describe interrelations between them including possibly their sequentially participation in the time domain [22]. However, a complex networks analysis can lead to a better understanding of the connections (links) between the components (nodes)—that is, the functional connectivity.

2 Experimental setup

In this work we have applied our analysis to a set of previously obtained and well studied data. The paradigm described in [11, 22] was designed to study brain electrical response from the incoming of a novel stimulus in a background of know stimuli. Stimuli (85 dB SPL) consisted of pure sine-wave tones of 700 Hz, with a duration of 75 ms (Standard tone) or 25 ms (Deviant tone), with 5 ms of fall/rise time. Trains of 3 tones were presented to subjects binaurally. The first tone of trains was Standard (p=0.5) or Deviant (p=0.5), while the other two tones were Standard. The inter-stimulus time was 300 ms, and the temporal separation between trains was 400 ms. A total of 400 stimuli trains were presented randomly. As can be seen in Figure 1, the signal (here for a single electrode) becomes self-coherent after stimulus onset. Figure 1 displays a plot of the inter-trial correlation coefficient function of the voltage time series for one electrode [37],

$$A_v(t_1, t_2) = \frac{\text{Cov}(t_1, t_2)}{\sigma_v(t_1) \sigma_v(t_2)}. \quad (1)$$

The coherence time of the signal, t_c , at a point t is the time it takes for the $A_v(t + t_c, t - t_c)$ to fall to 1/2. The coherence time can be visualized by inspecting A_v along lines of the form $(t_1, t_2) = (t, t) + t_c(-1, 1) = (t - t_c, t + t_c)$.

Sixteen healthy subjects (mean age 39 ± 11 years) participated in the study after having given their written consent. The subjects were instructed to ignore auditory stimuli while

they performed an irrelevant visual task (watching TV with the sound off). EEGs (bandpass 0-100 Hz) were recorded with a SynAmps amplifier (Neuroscan Inc) at a sampling rate of 500 Hz. A total of 30 electrodes were used: eighteen followed the 10-20 system without O1 and O2 (FP1, OZ, FP2, F7, F3, FZ, F4, F8, T3, C3, CZ, C4, T4, T5, P3, PZ, P4, T6), and twelve more electrodes (FC1, FC2, FT3, FT4, M1, M2, IM1, IM2, TP3, TP4, CP1 and CP2), all of them referenced to a nose electrode. Two extra electrodes were used to record vertical and horizontal ocular movements. Recordings were notch-filtered at 50 Hz. Epochs exceeding $\pm 100\mu\text{V}$ in EEG or in electro-oculogram were automatically rejected. Bandpass filtering (0.1-30 Hz) was performed, obtaining epochs of 400 ms, 100 ms before stimulus to 300 ms after it. Three subjects were excluded from the rest of the study because they did not have an identifiable MMN wave. In what follows, electrode voltage time series will be identified by $\phi_q(t_i)$, where the q index refers to the electrode number, and t_i to the time of sampling events.

3 Computation of the spatial Connectivity Matrix from EEG data

The network is constructed from the ERP data in three steps which we now describe.

1. Low Resolution Tomography (LORETA) [34] is employed to estimate the current densities within the brain from the measured electrode voltages on the scalp. According to our general understanding of the origin of bioelectric signals [36], the potentials we observe on the body surface are due to ionic current sources at the neuron membranes. As a result of these currents a charge density exists. More specifically, charges arise where impressed current density field lines are born or die. These charges are the source of the electrical potential at the scalp we measure. Therefore, given an accurate model of this forward process, we expect to be able to invert the operation and determine the cause (currents) from the effect (voltages). There is an important difficulty, however, as there is not a unique inverse solution: many patterns of current density can lead to the same

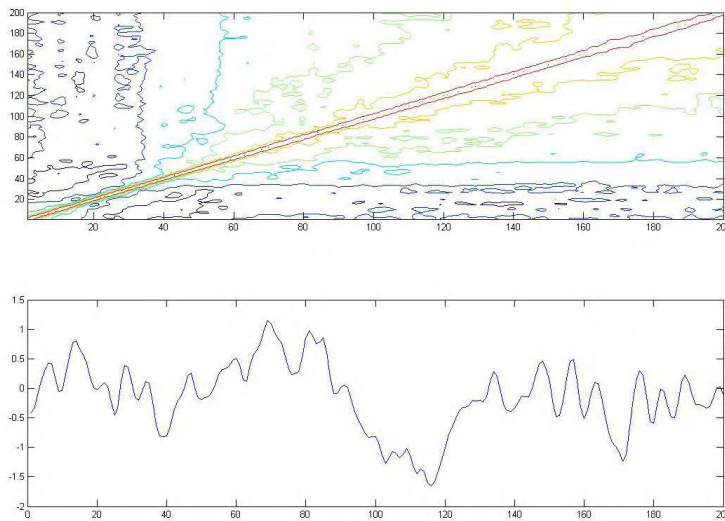


Figure 1: Top: Autocorrelation function of the ERP for different times (x and y axis denote time steps of 2 ms). This is computed from 300 trials (one subject), for electrode CZ. Note that the process is not stationary, as the statistics depend on time reference. Coherence times change are short before stimulus onset (at the 50 time step mark) and increase monotonically. Bottom: Average voltage over 300 trials.

measured electrode voltage pattern. For this reason it is not possible to exactly determine the current density from the electrode voltages. The LORETA algorithm picks out a current density solution with an adaptive resolution by searching for the smoothest of all possible current density solution maps J_n that satisfy boundary conditions derived from the position of cortical grey matter and the hippocampus of the Talairach human brain model. In the past five years, this tomographic approach has been used in several neuroscience studies (see for example [17, 23, 35, 10, 22]). The LORETA version used in this study searched for the sources of activation in 2394 voxels distributed in the Talairach human brain [34].

It will be useful to write here, in a simplified form, the tomographic equations. For each time step, the forward map K_{qn} , mapping current densities into electrode voltages, can be written as

$$\phi_q = \sum_n K_{qn} J_n, \quad (2)$$

and the inverse transformation T_{nq} , which is the inverse chosen by the LORETA algorithm, can be written as

$$\tilde{J}_n = \sum_q T_{nq} \phi_q. \quad (3)$$

We note here that we use a simplified notation, since J_n is actually a 3-vector. The LORETA inverse map gives an estimate of the current densities \tilde{J} from the electrode voltages. Note that KT is by definition of inverse the identity, while TK is in general not the identity. The ‘‘activation’’ of a voxel is defined to be the magnitude of the estimated current density,

$$I_n = \|\tilde{J}_n\| = \|T_{nq} \phi_q\|. \quad (4)$$

For each subject, for each time step of each 400 (400 ms long) trials and for each subject, the electrode data is transformed into a voxel current density magnitude using LORETA, producing 2394 voxel current density magnitude time series $I_n(t_i)$ for each trial. There are 100 Standard and 100 Deviant trials for each subject.

2. The second step is the computation of the inter-voxel correlation coefficient. The correlation coefficient c_{nm} between voxels n and m for a single trial, is defined to be the correlation coefficient of the activations over time.

$$c_{nm} = \frac{\langle I_n I_m \rangle_t - \langle I_n \rangle_t \langle I_m \rangle_t}{\sigma_n \sigma_m} = \langle S_n S_m \rangle_t \quad (5)$$

where $\langle \dots \rangle_t$ denotes a time average, $\sigma_n = \sqrt{\langle I_n^2 \rangle_t - \langle I_n \rangle_t^2}$ is the standard deviation of the activation, and $S_n(t_i) = [I_n(t_i) - \langle I_n \rangle_t] / \sigma_n$ is the demeaned and normalized activation signal. This coefficient can be interpreted as the cosine of the angle between the two activation time series vectors. The activation correlation coefficient used here is defined to be the average over all 100 trials of c_{nm} . We will use the notation \bar{c}_{nm} for the average activation correlation coefficient matrix.

3. As in [6], the links of the network are determined from the activation correlation coefficient matrix by applying a correlation threshold: when the absolute value of the correlation between voxels n and m is greater than the threshold r_c , the voxels are linked, otherwise the voxels are not linked. This defines the connectivity matrix, with entries equal to 1 (voxels are linked) or 0 (not linked),

$$A_{nm} = \begin{cases} 1 & \text{if } |\bar{c}_{nm}| > r_c \text{ and } n \neq m \\ 0 & \text{otherwise} \end{cases} \quad (6)$$

| r_c | $\langle k \rangle$ | $\langle C \rangle$ | $\langle C_{rand} \rangle$ | $\langle d \rangle$ | $\langle l \rangle$ | $\langle l_{rand} \rangle$ | l_{max} | T |
|-------|---------------------|---------------------|----------------------------|---------------------|---------------------|----------------------------|-----------|-----|
| 0.4 | 286 | 0.67 | 0.12 | 37 | 2.7 | 1.8 | 6 | 1 |
| 0.5 | 194 | 0.69 | 0.08 | 31 | 3.4 | 1.9 | 7 | 1 |
| 0.6 | 137 | 0.69 | 0.06 | 26 | 4.2 | 2.0 | 9 | 1 |
| 0.7 | 97 | 0.70 | 0.04 | 22 | 5.3 | 2.1 | 12 | 1 |
| 0.8 | 64 | 0.69 | 0.03 | 19 | 7.0 | 2.2 | 16 | 1 |
| 0.9 | 33 | 0.67 | 0.01 | 15 | 11.3 | 2.5 | 28 | 5 |

Table 1: Network parameters (see Section 5) for random uncorrelated electrode data. All number are dimensionless except for $\langle d \rangle$, which is in mm. The values for clustering index and average path length for an equivalent random network are also given.

Therefore, the nodes of the brain activation network are identified here with the voxels, while the links are specified by the connectivity matrix after thresholding (as in [6]). In the data set that is analyzed here a network is constructed for each subject for both deviant and standard conditions and for each threshold. This gives a total of 168 networks.

4 Analysis of correlations induced by the tomographic inverse transformation

One of the problems we encountered here is that the tomographic processing induces artificial correlations in the voxel activations. This is easily understood by a counting argument. In our test data set there were 30 data sources (the electrodes) and almost three thousand voxels, and the two spaces are related by a linear transformation. It is clear, then, that there will be correlations in the voxel activations even if the electrode data is randomly generated and fully de-correlated. Today it is possible to work with up to 256 electrodes, and this will certainly increase the effective tomographic resolution. Nevertheless, even with 256 electrodes the problem will remain and needs to be carefully analyzed. Here we provide only a preliminary analysis; we will leave a more detailed study of this issue to a future publication. In this paper we acknowledge that the network structure obtained is affected by the resolution problem, and for this reason we will focus only on the differences between two experimental setups. To first order, inversion induced correlation and network biases will then cancel.

While the true correlation coefficient matrix is not accessible, we can estimate the inversion induced correlations by analyzing two scenarios. The first one, already discussed, asks the question of what correlations are induced by the inversion if the electrode data is fully decorrelated. This scenario is appropriate for the analysis of decorrelated noise impact. Table 1 provides a summary of the network parameters from a Monte Carlo simulation.

The second is the scenario in which the original voxel signals are decorrelated: after forward mapping and then inversion, the resulting voxel cross-correlations can be used as an inversion induced background correlation threshold which can be used to estimate the inversion impact on the obtained connectivity matrix. This inversion induced correlation coefficient can in principle be computed from the tomographic equations. However, we recall here that the experimental connectivities have been obtained from the current activations (current density norm) in order to simplify data analysis. Nevertheless, for future reference we will compute here the inversion current correlation coefficient although is not directly applicable to the present analysis.

Suppose that the true current sources are given by J_n . It can easily be shown that if the true current sources are fully decorrelated, the cross-correlation of the estimated currents is

simply proportional to $R^t R$. After forward (K) and back (T) mapping, the estimated currents are given by

$$\tilde{J}_n = \sum_m (TK)_{nm} J_m \equiv \sum_m R_{nm} J_m. \quad (7)$$

We begin by calculating the average value of the estimated currents,

$$\begin{aligned} \langle \tilde{J}_i \rangle_t &= \langle \sum_n R_{in} J_n \rangle_t \\ &= \sum_n R_{in} \langle J_n \rangle_t \\ &= (RA)_i, \end{aligned} \quad (8)$$

where the vector A is defined by $A_n \equiv \langle J_n \rangle_t$. The cross-correlations are given by

$$\begin{aligned} \langle \tilde{J}_i \tilde{J}_j \rangle_t &= \langle \sum_n R_{in} J_n \sum_m R_{jm} J_m \rangle_t \\ &= \sum_{n,m} R_{in} R_{jm} \langle J_n J_m \rangle_t \\ &= \sum_{n,m} R_{in} \langle J_n J_m \rangle_t R_{mj}^t \\ &= (RBR^t)_{ij}, \end{aligned} \quad (9)$$

where the matrix B is defined by $B_{nm} \equiv \langle J_n J_m \rangle_t$, that is, the real cross-correlations. Similarly, the standard deviations are

$$\begin{aligned} \sigma_i &= \sqrt{\langle \tilde{J}_i^2 \rangle_t - \langle \tilde{J}_i \rangle_t^2} \\ &= \sqrt{(RBR^t)_{ii} - (RA)_i^2}. \end{aligned} \quad (10)$$

The cross correlation is given by

$$\begin{aligned} \tilde{C}_{ij} &= \frac{\langle \tilde{J}_i \tilde{J}_j \rangle_t - \langle \tilde{J}_i \rangle_t \langle \tilde{J}_j \rangle_t}{\sigma_i \sigma_j} \\ &= \frac{(RBR^t)_{ij} - (RA)_i (RA)_j}{\sqrt{(RBR^t)_{ii} - (RA)_i^2} \sqrt{(RBR^t)_{jj} - (RA)_j^2}}. \end{aligned} \quad (11)$$

Therefore, we see that the obtained correlation coefficient is a complex function of the biophysical correlations and the inversion matrices. As an example, consider the situation where the J_n are orthonormal and with zero mean, so that $\langle J_n J_m \rangle_t = \delta_{nm}$ and $\langle J_n \rangle_t = 0$. Then, $B = 1$ and $A = 0$ and

$$\langle \tilde{J}_i \rangle_t = (RA)_i = 0, \quad (12)$$

$$\langle \tilde{J}_i \tilde{J}_j \rangle_t = (RR^t)_{ij}, \quad (13)$$

$$\sigma_i = \sqrt{(RR^t)_{ii}}, \quad (14)$$

and

$$\tilde{C}_{ij} = \frac{(RR^t)_{ij}}{\sqrt{(RR^t)_{ii} (RR^t)_{jj}}} \equiv \tilde{C}_{ij}^0. \quad (15)$$

This quantity is in some sense the zero-point correlation in the estimated currents, since it is the correlation in the estimated currents when the actual currents having zero correlation. For this reason we expect this to be an indicative measure of the correlations induced by the inversion transform.

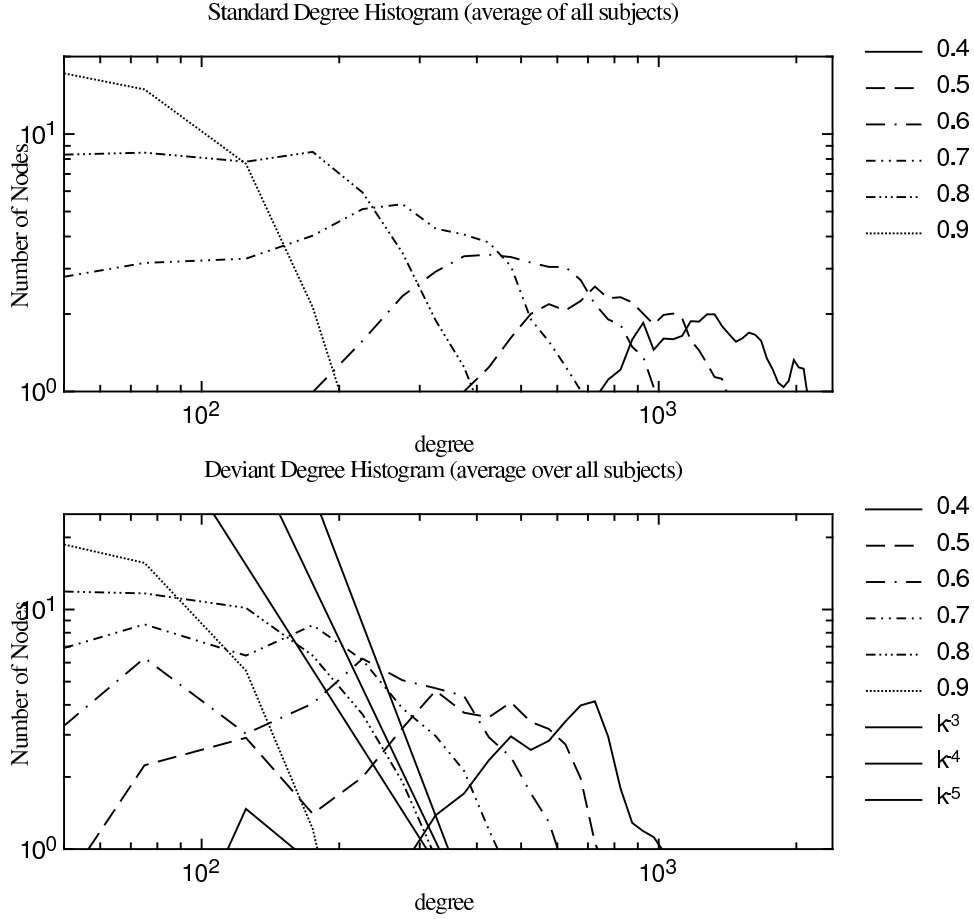


Figure 2: Degree distributions (node count as a function of degree) for the two experimental conditions (averaged over all subjects), and for different thresholds.

5 Network analysis

Once a network is defined by the connectivity matrix, we can study measures associated with the network[2, 6]. The following measures are computed for each node of a network:

- k_n is the degree of node n , the number of nodes linked to node n :

$$k_n = \sum_i A_{ni} = \sum_i A_{ni}A_{ni} = \sum_i A_{ni}A_{in} = A_{nn}^2 \quad (16)$$

- C_n is the cluster coefficient for node n , the ratio of the number of links between the neighbors of node n and the maximum possible number of links between the neighbors. With $\nu_n = \{m | A_{nm} = 1\}$ the set of neighbors of node n we can write the cluster coefficient as follows,

$$C_n = \frac{\sum_{i,j \in \nu_n} A_{ij}}{k_n(k_n - 1)} = \frac{A_{nn}^3}{k_n(k_n - 1)}. \quad (17)$$

Note that the second form is equivalent because the restricted sum of A_{ij} is the same as the unrestricted sum of $A_{ni}A_{ij}A_{jn}$ since either A_{ni} or A_{jn} is zero for the added elements of the sum and both are 1 for the original elements of the sum. The cluster coefficient is not defined for nodes with less than two neighbors.

- L_{nm} is the path length between nodes n and m , the minimum number of links required to travel through the network from node n to node m . The path length is undefined if no path between the nodes exists.

Based on these measures, the following parameters have been computed for each subject's connectivity matrix A and threshold r_c , and for each of the experimental conditions (Standard or Deviant tone):

- N , is the number of nodes with at least one link. This measure is not shown, since it does not deviate much (less than 1
- $\langle k \rangle$ is the average node degree for a particular network. The notation $\langle \dots \rangle$ indicates a network average,

$$\langle k \rangle = \frac{1}{N} \sum_n k_n = \frac{1}{N} \text{Tr}[A^2]. \quad (18)$$

- $\langle L \rangle$ is the average path length, an indicator of the connectedness of the network. Pairs of nodes without a connecting path are not included in the average.
- L_{max} is the maximal path length (the network perimeter). For a random network it is approximated by $L_{max} = \ln N / \ln \langle k \rangle$ [8].
- $\langle C \rangle$ is the average cluster coefficient, an indicator of the fraction of completed sub-networks. As described in [2], a common property of social networks is that cliques form, representing circle of friends or acquaintances in which every member knows every other member. This tendency to cluster is quantified by the clustering coefficient. For an equivalent random network $\langle C \rangle = \langle k \rangle / (N - 1)$.
- T is the number of *tribes*: we define a tribe as disjoint sub-network, i.e., one disconnected from the rest of the network. This can be easily computed from L_{mm} , by creating an associated matrix with ones everywhere except for disconnected voxel pairs (where the value is zero), and computing its rank.
- $\langle d \rangle$ is the average link physical length (in mm), which is not a topological measure but relevant nonetheless in the present study (although as pointed out in [6] cortex folding makes its interpretation more difficult),

For the computation of difference statistics given in Table 3, the difference of these measures for the Standard and Deviant networks is computed for each subject. Then the average and standard deviation are computed.

While more sophisticated tools in complex networks analysis are available, searching for the frequency of motifs, we concentrate in this first effort on a “classical” complex networks description.

Results for the characteristics of the networks associated with the brain electrical response to a Standard and Deviant tone without tomographic corrections are plotted in Figure 3. The degree distributions are provided in Figure 2, and the correlation coefficient difference distribution (link count) is provided in Figure ???. As can be seen there are marked differences between conditions in almost all studied parameters. The evaluation of the statistical differences between both conditions is summarized in Table 3, while the individual Standard and Deviant parameters are given in the summary Table 2. The number of links ($\langle k \rangle$), average physical distance ($\langle d \rangle$), and path length (averaged and maximum) present significant differences in the networks associated with the Standard and Deviant cases for all the studied correlation coefficients. The cluster coefficient and number of tribes are nearly constant over the range of thresholds studied. The number of tribes does increase for the largest threshold in the Standard case, although in all cases the network was formed by one large tribe with

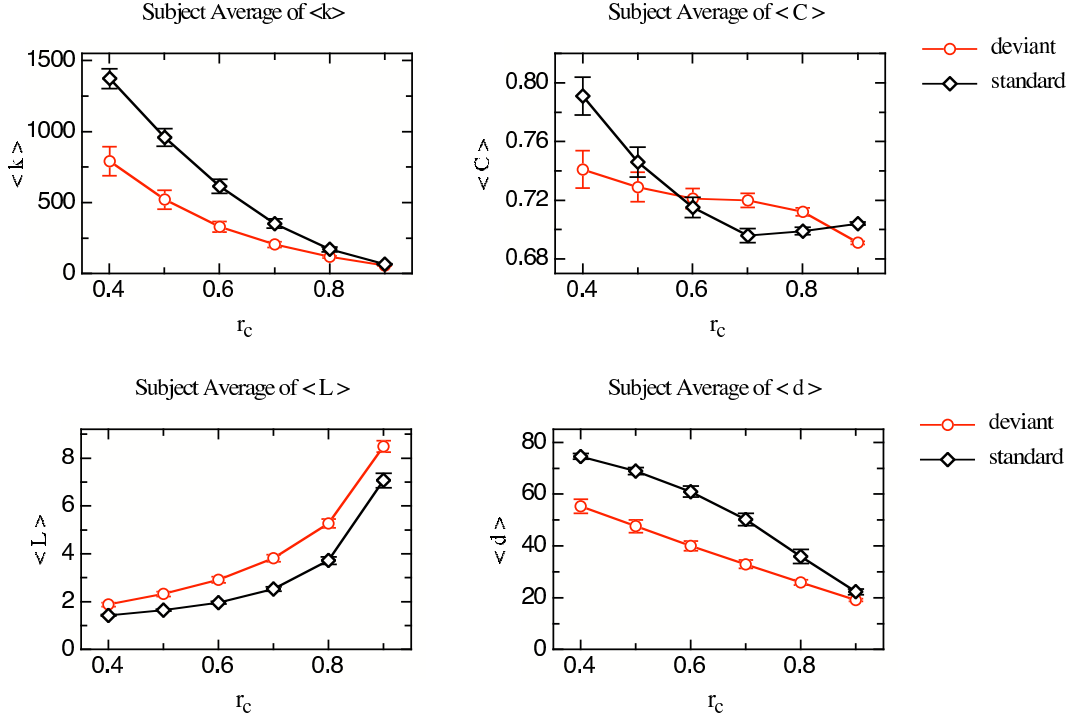


Figure 3: Average network parameters as a function of correlation threshold for all subjects and for the two experimental conditions— Standard and Deviant. The error bars reflect the uncertainty of the average values.

more than 99% of the nodes and the remaining nodes were not connected to each other. As can be seen in Table 4, the differences are statistically significant.

| r_c | $\langle k \rangle$ | $\langle C \rangle$ | $\langle C_{rand} \rangle$ | $\langle d \rangle$ | $\langle l \rangle$ | $\langle l_{rand} \rangle$ | l_{max} | T |
|-------|---------------------|---------------------|----------------------------|---------------------|---------------------|----------------------------|------------|-------|
| 0.4 | 1395 (255) | 0.80 (0.04) | 0.58 | 75 (4) | 1.4 (0.1) | 1.5 | 2.8 (0.4) | 1 (0) |
| 0.5 | 986 (222) | 0.75 (0.03) | 0.41 | 70 (5) | 1.6 (0.1) | 1.5 | 3.6 (0.5) | 1 (0) |
| 0.6 | 637 (170) | 0.72 (0.02) | 0.27 | 62 (6) | 1.9 (0.2) | 1.6 | 4.6 (0.5) | 1 (0) |
| 0.7 | 365 (120) | 0.70 (0.02) | 0.15 | 51 (9) | 2.5 (0.3) | 1.7 | 6.2 (0.8) | 2 (0) |
| 0.8 | 175 (64) | 0.70 (0.02) | 0.07 | 37 (10) | 3.6 (0.5) | 1.9 | 9.5 (1.3) | 2 (0) |
| 0.9 | 68 (13) | 0.70 (0.00) | 0.03 | 23 (4) | 6.9 (1.0) | 2.2 | 21.7 (3.2) | 9 (1) |

| r_c | $\langle k \rangle$ | $\langle C \rangle$ | $\langle C_{rand} \rangle$ | $\langle d \rangle$ | $\langle l \rangle$ | $\langle l_{rand} \rangle$ | l_{max} | T |
|-------|---------------------|---------------------|----------------------------|---------------------|---------------------|----------------------------|------------|-------|
| 0.4 | 723 (303) | 0.73 (0.04) | 0.30 | 54 (8) | 1.9 (0.3) | 1.6 | 3.8 (0.5) | 1 (0) |
| 0.5 | 477(198) | 0.73 (0.02) | 0.20 | 46 (8) | 2.4 (0.3) | 1.7 | 5.0 (0.6) | 1 (0) |
| 0.6 | 306 (111) | 0.72 (0.02) | 0.13 | 39 (6) | 3.0 (0.4) | 1.7 | 6.5 (0.8) | 1 (0) |
| 0.7 | 192 (60) | 0.72 (0.01) | 0.08 | 32 (5) | 3.9 (0.5) | 1.9 | 8.5 (0.7) | 1 (0) |
| 0.8 | 113 (24) | 0.71 (0.01) | 0.05 | 25 (3) | 5.4 (0.6) | 2.0 | 12.5 (1.0) | 1 (0) |
| 0.9 | 54 (9) | 0.69 (0.01) | 0.02 | 19 (2) | 8.6 (0.8) | 2.3 | 22.5 (2.6) | 2 (1) |

Table 2: Top: Network parameters for Standard data. Bottom: Network parameters for Deviant data. All numbers are dimensionless except for $\langle d \rangle$, which is in mm. The standard deviation of the data is shown in parenthesis—note that the mean uncertainty is smaller by the square root number of subjects. The values for clustering index and average path length for an equivalent random network are also given.

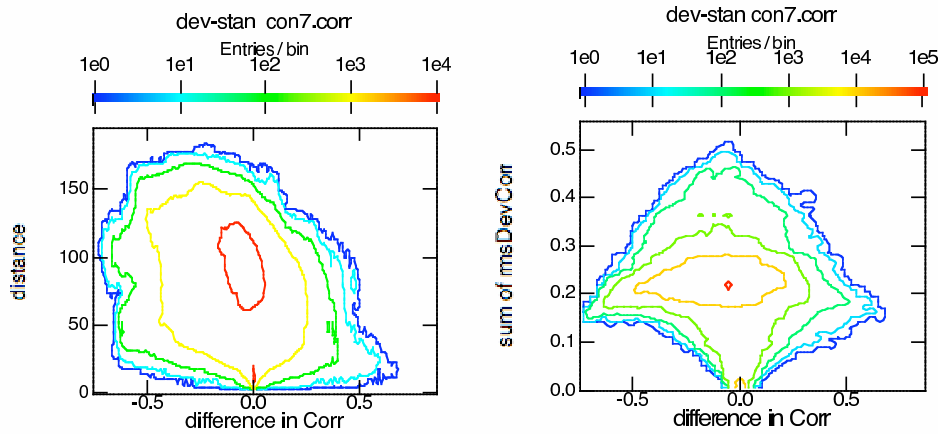


Figure 4: Left: Link count as a function of Correlation coefficient difference (Deviant minus Standard) and link length (mm) for one subject (the results are similar for all subjects). Right: as a function of standard deviation of the correlation coefficient over 100 trials.

| r_c | $\langle k \rangle$ | $\langle C \rangle$ | $\langle d \rangle$ | $\langle l \rangle$ | l_{max} | T |
|-------|---------------------|---------------------|---------------------|---------------------|------------|-------|
| 0.4 | 671 (276) | 0.07 (0.05) | 21 (8) | -0.5 (0.2) | -1.0 (0.7) | 0 (0) |
| 0.5 | 559 (189) | 0.03 (0.03) | 24 (7) | -0.7 (0.3) | -1.4 (0.6) | 0 (0) |
| 0.6 | 331 (122) | 0.00 (0.03) | 23 (7) | -1.1 (0.4) | -1.8 (0.8) | 0 (0) |
| 0.7 | 173 (85) | -0.02 (0.02) | 19 (7) | -1.4 (0.4) | -2.3 (0.7) | 1 (0) |
| 0.8 | 63 (48) | -0.01 (0.01) | 11 (8) | -1.7 (0.5) | -2.9 (1.3) | 1 (0) |
| 0.9 | 13 (11) | 0.01 (0.01) | 4 (4) | -1.7 (0.9) | -0.8 (3.7) | 7 (2) |

Table 3: Average difference of Standard and Deviant network measures (i.e., the subject by subject measured difference and then statistics). All numbers are dimensionless except for $\langle d \rangle$, which is in mm. Standard deviation of the data is shown in parenthesis—note that the mean uncertainty is reduced by one over the square root of the number of subjects.

Results for uncorrected data on voxels activated in the Mismatch Negativity process are shown in the Figure 5, which shows the correlations of all voxels with respect to selected reference voxels. Reference voxels are selected based on the results obtained in [22] with the same data set. As it can be seen, several important differences exist between networks for the Standard and Deviant responses. We can state the following:

- *Relative to the Deviant, the Standard network is more connected (with significantly more links at any given threshold), with longer links, with a shorter average and maximal path length.*
- *The increase in number of links in the Standard condition is greater at lower correlations, while at high thresholds the Standard network fragments more easily relative to the Deviant network.*

This seems to imply that the Standard-Deviant difference is characterized by a relative increase of long scale links at lower correlations in the Standard network, and also to a relative increase of short links at higher correlations in the Deviant network, which avoid fragmentation. Thus, we can say that the Standard network has a more “small world” character [45] than the deviant—especially at lower correlation coefficient thresholds. Both have shorter path lengths and perimeters than the random electrode data network (see Table 1). These can also be compared to Random network theory [2, 8]. The cluster coefficient for a random graph

| r_c | $\langle k \rangle$ | $\langle C \rangle$ | $\langle d \rangle$ | $\langle l \rangle$ | l_{max} | T |
|-------|---------------------|---------------------|---------------------|---------------------|-----------|----------|
| 0.4 | 5.87*** | 3.9*** | 7.98*** | -5.99*** | -5.38*** | 0 |
| 0.5 | 5.92*** | 2.6* | 8.96*** | -6.96*** | -6.50*** | 0 |
| 0.6 | 5.62*** | 0.17 | 9.12*** | -7.68*** | -6.57*** | 1 |
| 0.7 | 4.47*** | -3.14** | 6.78*** | -8.31*** | -7.31*** | 5.20*** |
| 0.8 | 2.94** | -3.69** | 3.55** | -7.71*** | -6.21*** | 11.08*** |
| 0.9 | 2.87** | 4.54*** | 2.86** | -4.44*** | -0.71 | 15.94*** |

Table 4: Student’s t-test statistics for the comparison between Standard and Deviant data. Here * $p < 0.05$, ** $p < 0.01$, *** $p < 0.001$.

(Erdos-Renyi) is simply given by $\langle C \rangle = \langle k \rangle / (N - 1)$, while according to [8], the average path length is given by

$$\langle L \rangle = \frac{\ln N - \gamma}{\ln \langle k \rangle}. \quad (19)$$

Although to some extent the same is true for the Deviant network, the results for the Standard case indicate, especially for low thresholds, a similar path length as would be expected from a random network, while the clustering index appears to be a factor of 2 greater. These results are similar to those obtained in [39] and rather different than those in [6]. They are also similar to analyses of the cat cortex [40] and the macaque visual cortex [12]. The obtained networks with low thresholds display “small world” properties, with high clustering and short path lengths [45]. This is especially true of the Standard network. It is interesting to note here that the clustering index is not very sensitive to the threshold, while the same is not true of the path length. This is consistent with the long but decreasing link lengths with increasing thresholds. Relatively low correlation links provide long scale connectivity.

With regards to scale free behavior, it is not readily apparent in either one, and in this sense our results are similar to those in [12, 39, 40] and different from those in [6]. The perturbation due to the inversion- induced correlations might mask such behavior to some extent, however, so it is not possible to make a definitive statement. It appears as if at higher correlations there Standard/Deviant differences are smaller—and thus of less physiological interest—with the exception of the number of tribes (disconnected sub- networks). As mentioned, there is a clear difference in the histograms of the networks especially at lower correlations (see Figure 2).

The Standard network is in essence much more connected and clustered at long scales, while at short scales the Deviant network appears to be more robust.

6 Discussion

In this paper we have provided a preliminary study of the statistical characteristics of brain networks associated with the brain electrical activity. We have addressed two fundamental questions. The first one is if complex network analysis can be used to discriminate, in a statistical significant way, between the chosen experimental conditions, and the stability of the measures across subjects. We have discussed the problems associated with tomographic inversion in preparation for network analysis, which made the outcome of the study less certain. The second question is if the results be interpreted physiologically. What can we learn about the spatial organization of brain information processing using a complex networks approach?

With regards to the first question, the results of this study show that network analysis can be used to discriminate between two different brain functional states with inter-subject stability, showing a potential relevance in the analysis EEG/MEG and ERPs/ERFs. Another

interesting result comes from the fact that, although parameters are highly dependent on the threshold used, the differences between Standard and Deviant data remain for the average number of links, average and maximal path length and average link physical length.

The first result that arises from the present study is that the number of links per voxel (node) in the Standard condition is significantly greater than in the Deviant condition—especially at lower correlation coefficient thresholds and longer scales. This result is, in principle, unexpected due to the fact that the brain electrical response to a Deviant tone elicits a greater activity mainly in supratemporal and frontal cortices [27, 31] indexed by MMN. However this result is consistent in all studied subjects and for all thresholds, and appears to be robust. This phenomenon appears to be related to the average link physical length, greater also in the Standard than in Deviant conditions, indicating a relative increase in longer scale connections in the Standard condition. The combination of both parameters (number of links and average connection distance) suggests a first physiological result:

- *The Standard condition presents higher connectivity at longer spatial scales and a strong “small world” character.*

This is consistent with the classical view of the brains electrical response to Deviant data. Supratemporal areas that are processing the characteristics of sound in the Standard conditions have to recruit nearby areas (also supratemporal ones) to perform the extra activity needed by the automatic detection of difference. Our results could also be interpreted in the framework of [13], where it is postulated that MMN is not a mechanism itself, but a non-reduced N1. Following this theory on MMN, supratemporal areas involved in the generation of the N1 would be the same as the areas that generate MMN. Links in the Deviant condition would be shorter because the main areas implicated in the production of MMN would be closer than in the attenuated N1. However, although Deviant data present less numerous and shorter links than Standard data, the Deviant network connects in a more efficient way all the cerebral areas as reflected by the greater number of “tribes” in the Standard network at higher thresholds.

As mentioned, these results are similar to those obtained in [39] and rather different than those in [6]—both working with fMRI data at much longer time scales.

In a previous analysis of the same data set [22] using Independent Component Analysis tomography, we found that the MMN is mediated by orchestrated activity of several spatially distributed brain sources located in the temporal, frontal, and parietal areas, which activate at distinct time intervals. When studying some of these areas several aspects became apparent. It was found that a right and a left supratemporal structure and the right inferior frontal cortex seem to be connected in the MMN condition (Deviant minus Standard) indicating that these structures could be related with the same brain function. Traditionally, the participation of temporal structures in the MMN ERP was associated with the analysis of the sound, whereas frontal structures were associated with the so-called “call to attention” [26, 31, 4]. However, in recent years, it has been found that these structures could be implied in the same functioning, as reflected by the fact that they could be present in the same independent component [22]. Moreover, primate studies have revealed that right inferior frontal structures are activated in response to a sound. The present study, which indicates that these areas are more connected in the response to a novel sound compared to Standard data, is consistent with previous findings and supports the idea that supratemporal and inferior frontal data work together in the processing of the differences between sounds. It is also clearly observable in Figure 5 that right frontal and parietal areas are linked together in deviant detection, which agrees with the hypothesis that both areas are connected in attentional processes [19, 20]. In this framework, it is stated that a spatially distributed set of neuronal groups that are activated coherently and are part of the same representation form an assembly [5]. In other terms, it could be described

as distributed local networks of neurons transiently linked by reciprocal dynamic connections, which supports functional integration [44].

The application of this approach could range from the basic studies determining the properties of networks associated with event related potentials or electroencephalography, to the study of pathological brain electrical responses, to biometrics. However, more studies have to be made in order to compare the information provided by an electrophysiology complex networks approach with information provided by other functional techniques (such as fMRI) and theoretical information to clearly validate this method. In particular, we plan to analyze elsewhere in more detail the impact of inversion in the network structure, as well as study other variants for the construction of the networks.

Acknowledgments

This work has been partly funded by the Starlab Kolmogorov program under the auspices of the FURNET network. G. Ruffini would like to thank Ed Rietman for valuable discussions, and in particular for pointing out the relevance of [6]. The authors wish to acknowledge support received from the Generalitat for support in the NECOM group (SGR2005) and the EU FP6 Sensation Integrated Project (FP6-507231) for partial support. Finally, the authors thank Carles Escera and Maria Dolores Polo (U. Barcelona) for data collection.

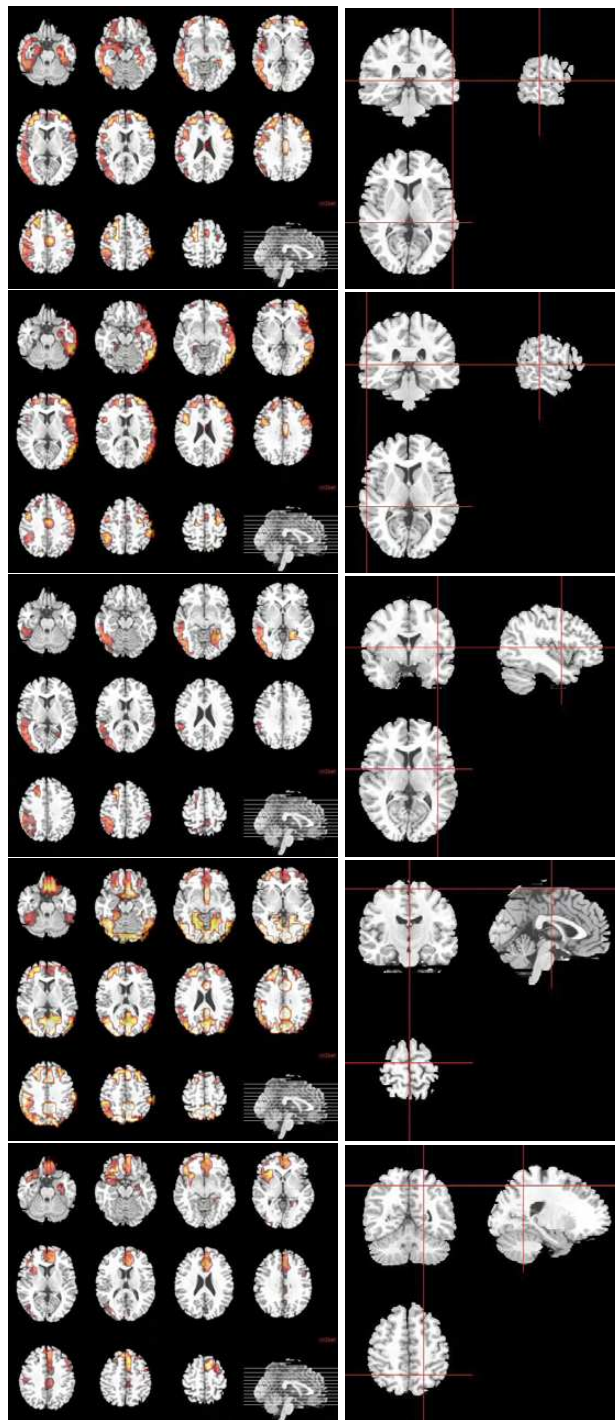


Figure 5: Deviant minus Standard correlations for the right supratemporal voxel (top), left supratemporal voxel, right inferior frontal voxel, central frontal voxel and right inferior parietal voxel (bottom).

References

- [1] Alain C, Woods DL, Knight RT. A distributed cortical network for auditory sensory memory in humans. *Brain Res.* 1998 Nov 23;812(1-2):23-37. Alain C, Arnott SR, Hevenor S, Graham S, Grady CL. "What" and "where" in the human auditory system. *Proc Natl Acad Sci U S A.* 2001 9:12301-12306. 5
- [2] Albert, R., Barabasi, A-L, Statistical mechanics of complex networks, *Rev. Mod. Phys.*, vol 74, pp 47–97, 2002. 4, 10, 11, 13
- [3] Bar-Yam, Y. and Epstein, R. Response of complex networks to stimuli. *Proc Natl Acad Sci USA* 2004; 101: 4341-4345. 5
- [4] Doeller, C.F., Opitz, B., Mecklinger, A., Krick, C., Reith, W., Schorfger, E., 2003. Pre-frontal cortex involvement in preattentive auditory deviance detection: neuroimaging and electrophysiological evidence. *NeuroImage* 20, 1270- 1282. 5, 15
- [5] Engel AK, Fries P, Singer W. Dynamic predictions: oscillations and synchrony in top-down processing. *Nat Rev Neurosci.* 2001, 2: 704-716. 15
- [6] Eguíluz VM, Chialvo DR, Cecchi GA, Baliki M, Apkarian AV .Scale-Free Brain Functional Networks. *Phys. Rev. Lett.* 94, 018102 (2005) 1, 4, 7, 8, 10, 11, 14, 15, 16
- [7] Friston, K.J. Models of brain function in neuroimaging. *Annu Rev Psychol.* 2005; 56:57-87. 4
- [8] Fronczak, A., Fronczak, P., Holyst, A., Average path length in random networks, *Phys. Rev. E* 70, 056110 (2004) 11, 13
- [9] Giard, M.H., Perrin, F., Perrier, J., Bouchet, P., 1990. Brain generators implicated in the processing of auditory stimulus deviance: a topographic event-related potential study. *Psychophysiology* 27, 627- 640. 5
- [10] Gomez, C, Marco J and Grau C. Preparatory visuo- motor cortical network of the contingent negativity variation estimated by current density. *Neuroimage* 20:216-224. 2003.
- [11] Grau C, Escera C, Yago E, Polo MD. Mismatch negativity and auditory sensory memory evaluation: a new faster paradigm. *Neuroreport.* 1998 Aug 3;9(11):2451-6. 7 5
- [12] Hilgetag, C.C., Burns, G.A.P.C., O'Neill, M.A., Scannell, J.W., Young, M.P., Anatomical connectivity defines the organization of clusters of cortical areas in the macaque monkey and the cat, *Phil Trans R Soc Lond B Biol Sci* 355, p. 91-110, 2000. 14
- [13] Jaaskelainen IP, Ahveninen J, Bonmassar G, Dale AM, Ilmoniemi RJ, Levanen S, Lin FH, May P, Melcher J, Stufflebeam S, Tiitinen H, Belliveau JW. Human posterior auditory cortex gates novel sounds to consciousness. *Proc Natl Acad Sci U S A.* 2004 Apr 27;101(17):6809-14. 5, 15
- [14] Javitt DC, Steinschneider M, Schroeder CE, Vaughan HG Jr, Arezzo JC. Detection of stimulus deviance within primate primary auditory cortex: intracortical mechanisms of mismatch negativity (MMN) generation. *Brain Res.* 1994 Dec 26;667 (2):192-200. 5
- [15] Kim, B.J., Geographical Coarse Graining of Complex Networks, *Physical Review Letters* Vol 93, Number 16, 15 Oct 2004.

- [16] Kircher TT, Rapp A, Grodd W, Buchkremer G, Weiskopf N, Lutzenberger W, Ackermann H, Mathiak K. Mismatch negativity responses in schizophrenia: a combined fMRI and whole-head MEG study. *Am J Psychiatry*. 2004; 161: 294-304. [5](#)
- [17] Kounios J, Smith RW, Yang W, Bachman P and D'Esposito M. Cognitive Association Formation in Human Memory Revealed by Spatiotemporal Brain Imaging. *Neuron* 29:297-306. 2001. [7](#)
- [18] Kandel R and Squire LR. Neuroscience: breaking down scientific barriers to the study of brain and mind. *Science*, 290:1113-1120. 2000. [4](#)
- [19] Kasai, K., Nakagome, K., Itoh, K., Koshida, I., Hata, A., Iwanami, A., Fukuda, M., Hiramatsu, K.I., Kato, N., 1999. Multiple generators in the auditory discrimination process in humans. *NeuroReport* 10, 2267- 2271. [5](#), [15](#)
- [20] Levänen, S., Ahonen, A., Hari, R., McEvoy, L., Sams, M., 1996. Deviant auditory stimuli activate human left and right auditory cortex differently. *Cereb. Cortex* 2, 288- 296. [5](#), [15](#)
- [21] Liasis, A., Towell, A., Alho, K., Boyd, S., 2001. Intracranial identification of an electric frontal-cortex response to auditory stimulus change: a case study. *Cognit. Brain Res.* 11, 227-233. [5](#)
- [22] Marco, J., Grau, C., Ruffini, G., Combined ICA- LORETA analysis of mismatch negativity, *Neuroimage* 2004. [1](#), [5](#), [7](#), [13](#), [15](#)
- [23] Mulert C, Gallinat J, Pascual-Marqui RD, Dorn H, Frick K, Schlattmann P, Mientus S, Herrmann WM and Winterer G. Reduced Event-Related Current Density in the Anterior Cingulate Cortex in Schizophrenia. *Neuroimage* 13:589-600. 2001. [7](#)
- [24] Müller, B.W., Jqpter, M., Jentzen, W., Mqlert, P., 2002. Cortical activation to auditory mismatch elicited by frequency deviant and complex novel sounds: a PET study. *NeuroImage* 17, 231- 239. [5](#)
- [25] Näätänen R, Gaillard AWK and Mantysalo S. (1978): Early selective-attention effect on evoked potential reinterpreted. *Acta Psychol* 42:313-329. [5](#)
- [26] Näätänen R, The role of attention in auditory information processing as revealed by event- related potentials and other brain measures of cognitive function. *Behav. Brain Sci.* 13, 201-288, 1990. [15](#)
- [27] Näätänen, R, *Attention and Brain Function*. Lawrence Erlaum Associates Publishers. Hillsdale, New Jersey, 1992. [5](#), [15](#)
- [28] Näätänen R, Alho K. Mismatch negativity—the measure for central sound representation accuracy. *Audiol Neurootol.* 1997 Sep-Oct;2(5):341-53. [5](#)
- [29] Näätänen R, Tervaniemi M, Sussman E, Paavilainen P, Winkler I. "Primitive intelligence" in the auditory cortex. *Trends Neurosci.* 2001 May;24(5):283-8. [5](#)
- [30] Nunez PL. *Neocortical Dynamics and Human EEG Rhythms*. New York: Oxford Univ Press. 1995. [4](#)
- [31] Opitz, B., Rinne, T., Mecklinger, A., Cramon, D.Y., Schrfger, E., 2002. Differential contribution of frontal and temporal cortices to auditory change detection: fMRI and ERP results. *NeuroImage* 15, 167-174. [5](#), [15](#)

- [32] Paavilainen P, Tiitinen H, Alho K, Naatanen R. Mismatch negativity to slight pitch changes outside strong attentional focus. *Biol Psychol.* 1993 Oct;37(1):23-41. [5](#)
- [33] Palla, G., Derenyi, I., Farkas, I., Vicsek, T., Uncovering the overlapping community structure of complex networks in nature and society, *Nature Letters*, Vol 435, 9 June 2005, p. 814.
- [34] Pascual-Marqui, R.D., Michel, C.M., Lehmann, D., 1994. Low resolution electromagnetic tomography: a new method for localizing electrical activity in the brain. *Int. J. Psychophysiol.* 18, 49. [6](#), [7](#)
- [35] Pizzagalli D, Pascual-Marqui RD, Nitschke JB, Oakes TR, Larson CL, Abercrombie HC, Schaefer SM, Koger JV, Benca RM and Davidson RJ. Anterior Cingulate Activity as a Predictor of Degree of Treatment Response in Major Depression: Evidence from Brain Electrical Tomography Analysis. *Am J Psychiatry* 158:405-415. 2001. [7](#)
- [36] Plonsey, R., *Bioelectric Phenomena*, McGraw-Hill, New York, 1969. [6](#)
- [37] Ramsay, J.O., Silverman, B.W., *Functional Data Analysis*, Springer 1997. [5](#)
- [38] Rosburg T., Effects of tone repetition on auditory evoked neuromagnetic fields. *Clin Neurophysiol.* 2004 Apr; 115 (4):898-905. [5](#)
- [39] Salvador, R., Suckling, J., Coleman, M.R., Pickard, J.D., Menon, D., Bullmore, E., Neurophysiological Architecture of Functional Magnetic Resonance Images of Human Brain, *Cerebral Cortex*, Sept 2005;15:1332–1342. [14](#), [15](#)
- [40] Scannell, J.W., Burns, G.A.P.C., Hilgetag, C.c., O’Neill, M.A., Young, M.P., The connective organization of the cortico-thalamic system of the cat, *Cereb Cortex* 9, p. 277–299, 1999. [14](#)
- [41] Tiitinen H, May P, Reinikainen K, Naatanen R. Attentive novelty detection in humans is governed by pre-attentive sensory memory. *Nature.* 1994 3:90-92. Tiitinen H, May P, Naatanen R. The transient 40-Hz response, mismatch negativity, and attentional processes in humans. *Prog Neuropsychopharmacol Biol Psychiatry.* 1997 Jul;21(5):751-71. [5](#)
- [42] Toga AW, Mazziotta JC. *Brain Mapping, the Methods*, San Diego: Academic Press Inc. 1996. [4](#)
- [43] Valverde, S., Sole, R., Network motifs in computational graphs: A case study in software architecture, *Phys Rev E* 72, 026107 (2005). [4](#)
- [44] Varela F, Lachaux JP, Rodriguez E, Martinerie J., The brainweb: phase synchronization and large-scale integration. *Nat Rev Neurosci.* 2001, 2 :229-239. [16](#)
- [45] Watts, D.J., Strogatz, S.G., Collective dynamics of “small world” networks, *Nature* 393, p. 440–442, 1998. [13](#), [14](#)